






UAV-Based Bistatic SAR-Imaging Using a Stationary Repeater

ALEXANDER GRATHWOHL  (Graduate Student Member, IEEE),
BENEDIKT MEINECKE  (Graduate Student Member, IEEE), **MARIUS WIDMANN** ,
JULIAN KANZ  (Graduate Student Member, IEEE), AND **CHRISTIAN WALDSCHMIDT**  (Fellow, IEEE)
(Regular Paper)

Institute of Microwave Engineering, Ulm University, 89081 Ulm, Germany

CORRESPONDING AUTHORS: Alexander Grathwohl; Benedikt Meinecke (e-mail: alexander.grathwohl@uni-ulm.de; meinecke@ieee.org).

This work was supported by Deutsche Forschungsgemeinschaft (DFG, German Research Foundation) under GRK 2680-Project-ID 437847244 and Project-ID 424265908. (Alexander Grathwohl and Benedikt Meinecke contributed equally to this work.)

This work did not involve human subjects or animals in its research.

ABSTRACT Synthetic aperture radar (SAR) is an established technique for high-resolution radar imaging relying on the ego-motion of the radar. The long coherent integration time of the radar in conjunction with a linear or circular trajectory enables the illumination of targets under different observation angles leading to robustness against short-time interference signals. The use of a bistatic setup to simultaneously acquire multiple observation angles further increases the aforementioned benefits. In this work, a bistatic SAR system using an active repeater is proposed, in the following called Bistatic Repeater-SAR (BR-SAR). In BR-SAR the repeater acts as a second observer providing a bistatic path with low system cost and hardware effort. This article discusses the BR-SAR approach with all signal processing and hardware considerations necessary to build the bistatic radar system. This includes a description of the full system and signal chain with a focus on the signal separation and evaluation of both monostatic and bistatic signals and the subsequent SAR processing. The approach is verified via simulations and measurements, in which conventional SAR is compared to the proposed BR-SAR system. Hardware effects leading to a deteriorated system performance of the bistatic system are analyzed and countermeasures are discussed and implemented. Finally, the benefits of the bistatic system are demonstrated based on a realistic measurement scenario.

INDEX TERMS UAV, SAR, bistatic, radar, repeater, system, coherency, mixer.

I. INTRODUCTION

Synthetic aperture radar (SAR) is widely used in remote sensing due to the high achievable resolution [1]. Applications of SAR are, among others, ship surveillance [2], earthquake damage assessment [3], and tomography [4], [5].

Further developments in this area include bistatic SAR systems which enable new fields of operation like single-pass interferometry [6], observation of dynamic processes and vegetation, or single-pass tomography [7]. Bistatic radar has been used prior to space-borne missions in applications such as the estimation of soil moisture [8], [9] and wind speed [10]. Additionally, bistatic radar can be used to minimize shadowing effects [11] and provide more polarimetric parameters and

three-dimensional displacement vectors [12], [13] enhancing image interpretation.

The spatial separation of transmitting and receiving units, e.g. on multiple satellites, places high demands on the synchronization within the system. Coherency in these networks can be achieved by transmitting a reference signal [12], [14], [15] or by operating incoherent sensor nodes in a coherent manner using digital processing [16].

The complexity of synchronization can be circumvented using a monostatic radar together with a repeater instead of two radar systems. The repeater receives the signal from the scene, processes it, and transmits it back to the monostatic receiver [17]. The down-conversion of the bistatic signal is

coherently performed in the monostatic receiver and both mono- and bistatic signals are processed within the same system.

Repeaters have been used before in radar networks to achieve coherency between nodes without requiring complex synchronization. Applications range from direction-of-arrival and velocity estimation [18], [19], [20] to locating repeater nodes within a radar network [21]. Bistatic SAR experiments were performed by moving either the radar [22] or the repeater [23]. In these works, the repeater solely amplifies the signal before sending it back.

Recently, the use of unmanned aerial vehicles (UAVs) as a platform for radar imaging has increased due to technological advances and higher availability of these systems [24], [25], [26], [27]. Compared to airborne systems on larger aircrafts or spaceborne systems, unmanned aerial vehicle (UAV)-based radar offers a higher flexibility in operation. Monostatic SAR imaging with UAVs already showed promising results in detecting buried objects [28], [29], determining snow depths [30], and in archaeological surveys [31]. Time-domain methods in particular have proven to be suitable for UAV-based SAR imaging due to the absence of simplifying assumptions compared to frequency-domain methods [25], [32]. Considering different viewing angles, imaging can be further improved as different angles complement each other [12]. This can be achieved by using a bistatic acquisition geometry.

Using a repeater, mono- and bistatic paths are measured simultaneously. If their ranges are similar, they can not be distinguished at the receiver. A separation can be achieved by strictly constraining the measurement geometry to guarantee different ranges. To take advantage of the flexibility of UAV flight paths, another means of separation is therefore required. An additional frequency modulation at the repeater represents a solution to this challenge. Using this modulation, the mono- and bistatic paths are separable and both signals can be received and processed at the same time [18].

In this article, a UAV-borne SAR system based on a frequency-modulated continuous-wave (FMCW) radar [33] is extended by a repeater to allow both monostatic and bistatic measurements of a scene. This approach circumvents the high demands on synchronization when using two radar systems for bistatic data acquisition. In contrast to [22], [23], the signal is not only amplified at the repeater but also frequency modulated. Due to the proportionality of frequency and range in FMCW processing, the bistatic signal becomes separable from the monostatic one. However, modulating the signal at the repeater places demands on digital signal processing. The required adaptations are presented in this work, enabling both bistatic and monostatic SAR images.

A detailed description of the radar signals and the required signal processing is given in Section II. Section III shows simulation results of the proposed implementation, which are validated by measurements in Section IV.

II. THEORY

In the following, first, detailed definitions of all signals involved in basic FMCW radar and SAR processing are given.

Afterwards, the definitions are extended for bistatic imaging using a repeater.

A. FMCW RADAR EVALUATION

The frequency ramp sent out by an FMCW radar is described by [34]

$$f_T(t) = f_0 + \frac{B}{T}t = f_0 + k_r t, \quad (1)$$

where f_0 is the start frequency of the ramp, B is the bandwidth, T is the ramp time and k_r is the slope of the ramp. Its phase can be described by

$$\phi_T(t) = 2\pi \int_0^t f_T(\tau) d\tau = 2\pi f_0 t + \pi k_r t^2 - \phi_0. \quad (2)$$

Assuming a single target, the signal is reflected at the target back to the radar. The received signal is equal to the transmitted one, but delayed by Δt due to the distance to the target. The signal phase is

$$\phi_R(t) = 2\pi f_0(t - \Delta t) + \pi k_r(t - \Delta t)^2 - \phi_0. \quad (3)$$

By mixing the transmit and receive signals, the relevant target information is extracted as the phase difference

$$\Delta\phi(t) = \phi_T(t) - \phi_R(t) = 2\pi f_0 \Delta t + 2\pi k_r t \Delta t - \underbrace{\pi k_r \Delta t^2}_{\text{small}}. \quad (4)$$

If the target is located at a radar range R and moves with a relative velocity of v away from the sensor, the time delay can be described by

$$\Delta t = \frac{2}{c_0}(R + vt), \quad (5)$$

which leads to

$$\Delta\phi(t) \approx \frac{4\pi}{c_0} \left(f_0 R + f_0 vt + k_r t R + \underbrace{k_r vt^2}_{\text{small}} \right). \quad (6)$$

This corresponds to a beat-frequency of

$$f_B = \frac{1}{2\pi} \frac{\partial \Delta\phi(t)}{\partial t} \approx \frac{2f_0}{c_0} v + \frac{2k_r}{c_0} R. \quad (7)$$

If $f_0 = 1 \text{ GHz}$, $k_r = 3 \times 10^{12} \text{ s}^{-2}$, this leads to

$$\frac{2f_0}{c_0} v \ll \frac{2k_r}{c_0} R, \quad (8)$$

if v and R are in the same order of magnitude. The influence of the velocity of a target is negligible. In that case, the beat-frequency can be estimated to

$$f_B(R) = \frac{2k_r}{c_0} R. \quad (9)$$

The beat signal is digitized using an analog-to-digital converter (ADC) before further processing. The radar does not use an Inphase/Quadrature (IQ) mixer, the signal is therefore real-valued. For clarity, continuous-time signals are noted by $s(t)$ and their discrete-time counterparts are noted by $s[t]$ with $k = t f_s \in \{0, \dots, N - 1\}$, where f_s is the sampling frequency

and N is the size of the signal vector. The discrete-time beat signal can then be written as

$$s_B[t] = \text{Re} \left(e^{j2\pi \left(\frac{2k_r R}{c_0} \right) t} \right). \quad (10)$$

For further processing, a Hann-window ($w[k], 0 \leq k < N$) is applied, followed by zeropadding. This results in a new signal length of N_0 . The range information $S_B[f_r]$ can then be extracted by applying a Fourier transform to the zero-padded and windowed discrete-time beat signal $s_{B,0}[t]$:

$$s_{B,0} \left[\frac{k}{f_s} \right] = \begin{cases} s_B \left[\frac{k}{f_s} \right] \cdot w[k] & \text{if } k < N \\ 0 & \text{if } k \geq N \end{cases} \quad (11)$$

$$S_B[f_r] = \sum_{k=0}^{N_0-1} s_{B,0} \left[\frac{k}{f_s} \right] \cdot e^{-j \frac{2\pi k f_r}{f_s}} \quad (12)$$

This step of extracting the range information is referred to as range compression. It is commonly implemented using a fast Fourier transform (FFT). After range compression, the single target that was assumed at the beginning of this section results in a peak in $S_B[f_r]$ at

$$f_r(R) = f_B(R). \quad (13)$$

B. PHASE OF A POINT TARGET

Employing synthetic aperture processing, high-resolution images of a static scene can be obtained. The radar system is moved along a trajectory, periodically recording measurements. As long as the position of the radar sensor is known with sufficiently high precision, an estimate of the radar cross-section (RCS) of points in the scene can be calculated.

For the following derivation, a single ideal point target at a static position is assumed. Due to the moving radar sensor, the distance R_m between radar and target is dependent on the measurement index m . The true beat-frequency is also dependent on m and is therefore explicitly written as $f_B(R_m)$.

First, the range information from each radar measurement m is obtained via range compression, as stated above. For the given single point target, the range-compressed signal is [32]

$$S_{B,m}[f_r] = T \text{sinc} \left[T \left(f_r - \frac{2k_r R_m}{c_0} \right) \right] \cdot \exp \left[j\phi_B(f_r, R_m) \right] \quad (14)$$

with

$$\phi_B(f, r) = \frac{4\pi f_0 r}{c_0} - \pi T f + \frac{2\pi T k_r r}{c_0} - \frac{4\pi f r}{c_0} + \frac{4\pi k_r r^2}{c_0^2}. \quad (15)$$

A continuously evaluable function is given by

$$S_{B,m}(R) = S_{B,m}[f_r = f_B(R)], \quad (16)$$

which includes interpolation for the right expression. Relying on sufficient zeropadding in the range compression, linear

interpolation between the neighboring samples in $S_{B,m}[f_r]$ is used.

The maximum amplitude of the sinc is reached at the true beat-frequency of the point target for every measurement. With (13) and (9), the expected phase of the point target can be derived:

$$\begin{aligned} \phi_e(R_m) &= \phi_B(f_B(R_m), R_m) \\ &= \frac{4\pi f_0 R_m}{c_0} - \frac{4\pi k_r R_m^2}{c_0^2} \end{aligned} \quad (17)$$

C. BACKPROJECTION

Synthetic aperture processing can be achieved using a variety of approaches. These can mostly be divided into time-domain and spatial frequency-domain methods [35], [36]. Frequency-domain methods offer the advantage of lower computational complexity due to their relation to the FFT, but they impose strict requirements on the measurement, such as linear trajectories or equidistant measurements. Although more computationally expensive, time-domain methods such as backprojection (BP) iteratively process all measurement data and therefore rely on very few assumptions regarding the measurement geometry [33]. This work relies on BP because of the highly-nonlinear flight trajectories of multicopters and the additional degree of freedom regarding the measurement setup.

BP processes radar measurements and populates a grid of pixels, usually on a plane or in a volume. Due to its iterative nature, it can be mathematically described in terms of its operation on a single pixel at a position $\mathbf{x}_0 = [x_0, y_0, z_0]$. After processing all measurements m , the resulting pixel value $A(\mathbf{x}_0)$ is given by [32]

$$A(\mathbf{x}_0) = \sum_m S_{B,m}(R_m) \exp \left[-j\phi_e(R_m) \right], \quad (18)$$

where

$$R_m = n_1 \|\mathbf{x}_0 - \mathbf{x}_{a,m}\|_2 \quad (19)$$

is the range from antenna to pixel and $\mathbf{x}_{a,m}$ is the position of the radar antenna for measurement m .

The theoretically expected phase $\phi_e(R_m)$ of a point target is used to compensate the phase extracted from the range information. If \mathbf{x}_0 contains a target, $A(\mathbf{x}_0)$ becomes a coherent sum over complex values resulting in a value with large amplitude. If there is no target, the summation is not coherent and the result is of much lower amplitude. Therefore, the SAR image is a representation of the RCS of the investigated area sampled at the pixel coordinates.

D. FMCW WITH REPEATER

This work extends the FMCW radar by a repeater element, enabling the evaluation of a bistatic path. The repeater consists of a transmit and receive antenna as well as an amplifier and mixer. The mixer is used to shift the incoming signal in frequency by f_{mod} . This requires a single-sideband mixer, otherwise shifting by $\pm f_{\text{mod}}$ would occur. The signal applied

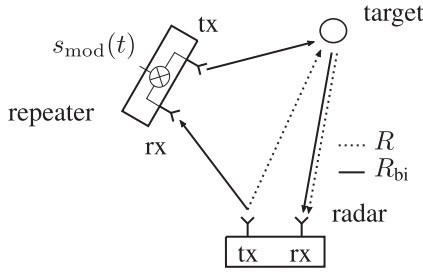


FIGURE 1. Schematic representation of a bistatic FMCW radar system with repeater to generate the bistatic path R_{bi} . The monostatic path R is also depicted as a dotted line for reference.

to the mixer in the repeater is given as

$$s_{\text{mod}}(t) = \hat{s}_{\text{mod}} \exp(j2\pi f_{\text{mod}}t + \varphi_{\text{mod},0}(\gamma)), \quad (20)$$

where \hat{s}_{mod} is the amplitude of the modulation signal, f_{mod} the modulation frequency, and $\varphi_{\text{mod},0}(\gamma)$ the modulation phase at the starting time of radar transmission. Since the repeater is independent of the radar sensor, the start phase $\varphi_{\text{mod},0}(\gamma)$ depends on the global start time γ of the FMCW chirp. Due to the modulation within the repeater, the mathematical description for an FMCW radar from Section II-A needs to be extended, see [18] for more details. The frequency of the receive ramp is changed via the repeater to

$$f_{\text{R}}(t) = f_{\text{T}}(t) - f_{\text{mod}}. \quad (21)$$

As a consequence, the beat frequency in the linear region of each ramp is given as

$$f_{\text{B}} = f_{\text{T}}(t) - f_{\text{R}}(t) = \frac{2k_{\text{r}}}{c_0} R_{\text{bi}} + f_{\text{mod}}. \quad (22)$$

A target at a bistatic range R_{bi} is therefore additionally shifted by

$$R_{\text{shift}} = +f_{\text{mod}} \frac{c_0}{2k_{\text{r}}}. \quad (23)$$

The virtual received range for a bistatically received signal is then given as

$$\tilde{R}_{\text{bi}} = R_{\text{bi}} + R_{\text{shift}}. \quad (24)$$

The ramp frequency shift via the bistatic path is advantageous, because it enables the separation of monostatic and bistatic signals with similar physical ranges by virtually shifting the bistatic target response in range. Without the shift, monostatic and bistatic signal components at similar ranges interfere and lead to poor imaging quality after BP processing. This is especially relevant for complex trajectory geometries now possible using UAVs, since the separation of mono- and bistatic receive signals in range would place significant restrictions on the geometries. An example setup of the bistatic radar system including both signal paths is depicted in Fig. 1.

The bistatic path length R_{bi} consists of the total distance between radar, repeater and target, as depicted in Fig. 1. The transmission delay caused by the signal run time within the repeater further increases R_{bi} and needs to be included.

E. EXTENDED BACKPROJECTION

The FMCW model for bistatic measurements necessitates an extension of the BP algorithm. As described in the previous section, the bistatic range of the target measured by the FMCW radar is shifted via the repeater. The extended processing must take into account this range shift.

While the discrete-time monostatic signal can be described by

$$s_{\text{B}}[t] = A \cos(2\pi f_0 \Delta t + 2\pi k_{\text{r}} t \Delta t - \pi k_{\text{r}} \Delta t^2), \quad (25)$$

the bistatic signal includes an additional phase term due to the modulation:

$$s_{\text{B,bi}}[t] = A \cos(2\pi f_0 \Delta t_{\text{bi}} + 2\pi k_{\text{r}} t \Delta t_{\text{bi}} - \pi k_{\text{r}} \Delta t_{\text{bi}}^2 + 2\pi f_{\text{mod}} t + \varphi_{\text{mod},0}(\gamma)) \quad (26)$$

Contrary to the start phase of the transmitted radar chirp, $\varphi_{\text{mod},0}(\gamma)$ is not compensated in the receiver. For coherent processing, it must therefore be calculated based on the global time for every chirp. Due to tolerances in manufacturing and measurement inaccuracies, the repeater phase cannot be calculated directly. It needs to be estimated from f_{mod} , γ , as well as measurement data of a stationary point target to account for drifts.

To allow bistatic targets to be processed using classic BP, the signal is digitally demodulated:

$$\begin{aligned} \tilde{s}_{\text{B,bi,demod}}[t] &= (s_{\text{B}}[t] + s_{\text{B,bi}}[t]) \cdot \exp[-j(2\pi f_{\text{mod}} t + \varphi_{\text{mod},0}(\gamma))] \\ &= \frac{A}{2} \exp[j(\pi f_0 \Delta t_{\text{bi}} + 2\pi k_{\text{r}} t \Delta t_{\text{bi}} - \pi k_{\text{r}} \Delta t_{\text{bi}}^2)] + \xi[t], \end{aligned} \quad (27)$$

where $\xi[t]$ represents modulation products irrelevant to the following BP.

At the top of Fig. 2, the periodic spectrum $S_{\text{B}}(f)$ of the sampled base band signal including both mono- and bistatic components is displayed. Using the demodulation, the spectrum is shifted towards negative frequencies, such that the bistatic response is now positioned where the monostatic response was previously located. The resulting spectrum is displayed at the bottom of Fig. 2. In the demodulated spectrum $S_{\text{B,dem}}(f)$, aliasing introduces a copy of the bistatic signal in the base band, which is of no concern, since its location corresponds to distances not evaluated during BP. Thus, $\tilde{s}_{\text{B,bi,demod}}[t]$ can be processed with standard BP if R_{bi} is known.

III. SIMULATIONS

In this section, the proposed extensions to FMCW and BP are verified using simulations. The radar parameters assumed for simulation and measurements are equal to allow for a reliable prediction of results. All parameters are listed in Table 1. The modulation frequency in the repeater is assumed to be $f_{\text{mod}} = 1.2$ MHz. First, the interference effects that occur

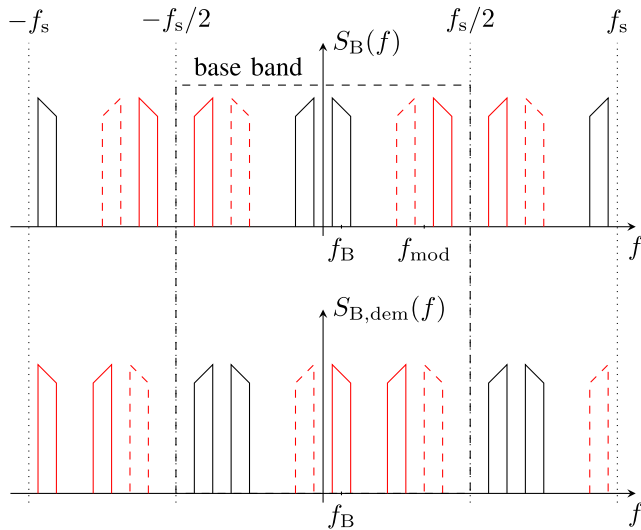


FIGURE 2. Spectrum of sampled bistatic upper sideband (red, solid), lower sideband (red, dashed), and monostatic (black) received signal before and after demodulation.

TABLE 1. FMCW Radar Technical Parameters for Simulations and Measurements

parameter	symbol	value
chirp start frequency	f_0	1 GHz
chirp stop frequency		4 GHz
bandwidth	B	3 GHz
chirp duration	T	1 ms
chirp rate	k_r	$3 \frac{\text{THz}}{\text{s}}$
baseband sampling rate	f_s	3.6 MHz

without a frequency modulation in the repeater elements are investigated. This is followed by the simulation of the extended backprojection algorithm from Section II-E.

A. BENEFIT OF SIGNAL MODULATION VIA REPEATER

To demonstrate the degrading effect of interference, a repeater without modulation is assumed. A grid of 7×7 point targets with 50 cm separation in x and y direction is simulated. The radar system moves in a straight line from $(x, y) = (-5 \text{ m}, -5 \text{ m})$ to $(-5 \text{ m}, 10 \text{ m})$, while the repeater is stationary at $(0 \text{ m}, 4 \text{ m})$.

Both mono- and bistatic target responses are received by the radar. As the area is populated with many targets, there is a large variety in target ranges. Mono- and bistatic target responses occur at similar ranges which are superimposed at the receiving radar. Without modulation, no separation of the received signals is possible, leading to interference.

For bistatic signals, the expected receive power is reduced compared to monostatic signals. This is due to a larger bistatic range ($R_{bi} > R$) and losses introduced by the repeater element itself. In this simulation, a power difference of 13 dB is assumed.

Monostatic processing using classic BP still gives a focused SAR image, because the monostatic signal power is

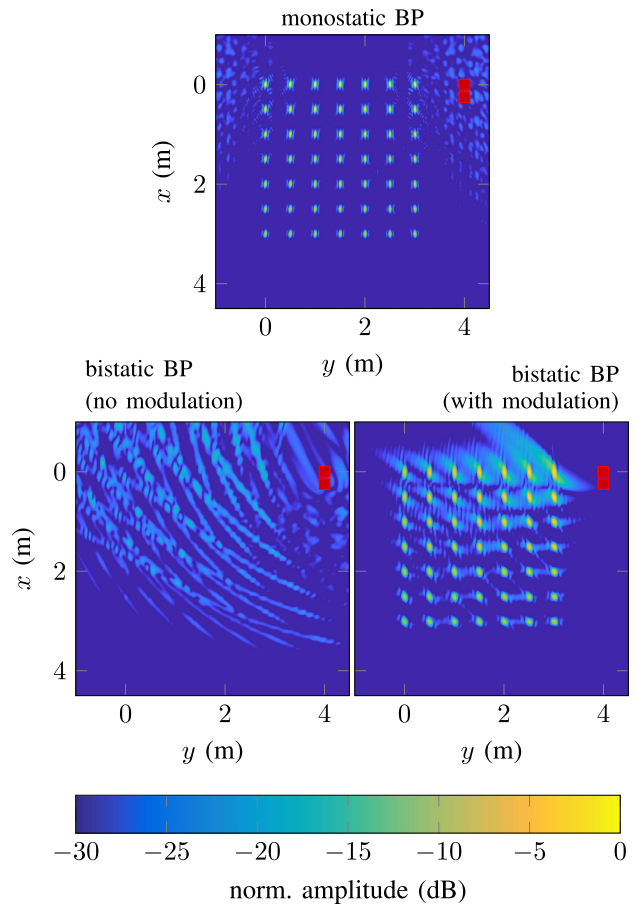


FIGURE 3. Monostatic and bistatic BP using a repeater with and without modulation. The position of the repeater is static and marked in red. A linear radar trajectory from $(x, y) = (-5 \text{ m}, -5 \text{ m})$ to $(-5 \text{ m}, 10 \text{ m})$ was simulated. A power difference of 13 dB between monostatic and bistatic received signals was assumed.

significantly above the bistatic one. All point targets can be focused, as is visible on the top of Fig. 3. In contrast, bistatic processing with $f_{mod} = 0$ yields a degraded SAR image, as can be seen on the bottom left of the same Figure. The monostatic signal masks the bistatic signal of interest, significantly reducing the coherency of the summation in BP for bistatic target responses.

A modulation in the repeater as described in Section II-D avoids this masking, by separating mono- and bistatic responses in virtual range as described in (24). Bistatic BP after demodulation then gives a significantly improved result which is visible in the bottom right of Fig. 3.

B. BISTATIC SIMULATION - SINGLE-TARGET CASE

Introducing a modulation in the repeater element leads to a shift in the range-compressed signal, which is later removed by digital demodulation. For a single-target scenario, simulated range-compressed data before and after demodulation can be seen in Fig. 4. A linear measurement trajectory from $(x, y) = (0 \text{ m}, -0.1 \text{ m})$ to $(0 \text{ m}, -12 \text{ m})$ and a single point target at $(6.85 \text{ m}, -5.46 \text{ m})$ were simulated. Here, only a bistatic

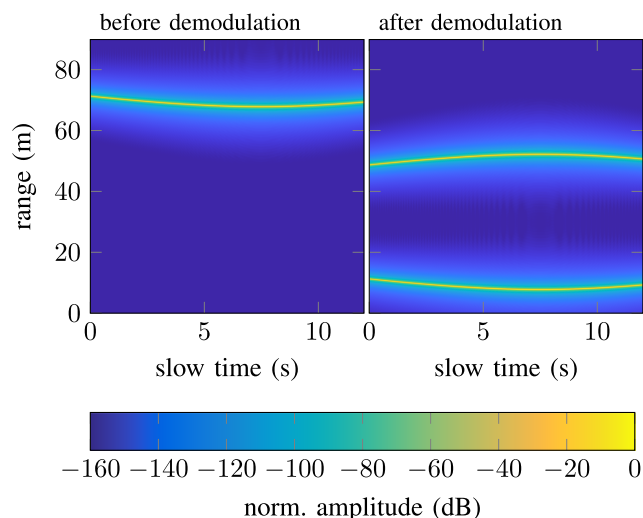


FIGURE 4. Range-compression of received bistatic signal of a single target, before and after demodulation.

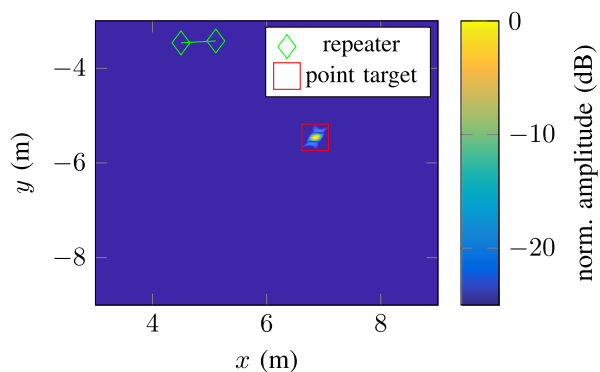


FIGURE 5. Bistatic SAR image of a simulated single-target case. A radar trajectory from $(x, y) = (0 \text{ m}, -0.1 \text{ m})$ to $(0 \text{ m}, -12 \text{ m})$ and a target at $(6.85 \text{ m}, -5.46 \text{ m})$ were simulated.

signal is assumed. The curvature of the target response is due to the measurement geometry with changing distances between radar sensor, repeater, and target. Aliasing leads to a second curve at higher ranges, as shown in Fig. 2.

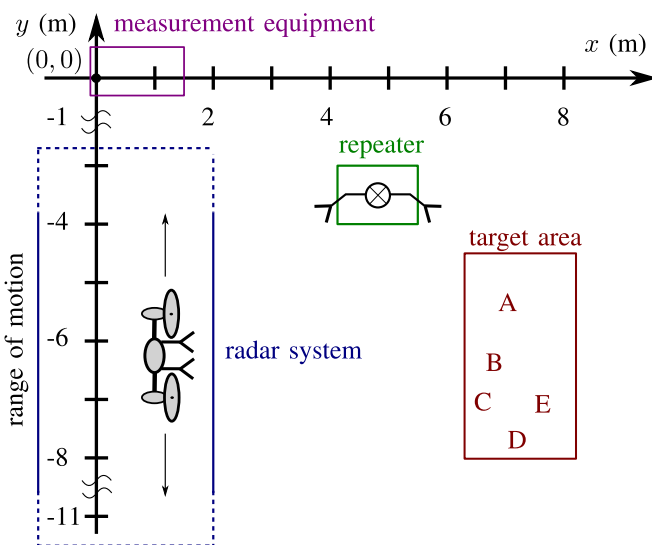
Using the precisely known trajectory and stationary repeater antenna positions from the simulation, BP is applied. In this idealized example, the resulting image (Fig. 5) is free of clutter and interference. The single simulated target is clearly visible at the expected position. This confirms that bistatic SAR including modulation is possible under ideal conditions.

IV. MEASUREMENT RESULTS

The preceding theory and simulations are validated via outdoor measurements using an UAV equipped with an FMCW radar and a static repeater placed in the scene, see Fig. 6. The target area contains a large metal cylinder [A] and, optionally, various other metal objects [B-E]. A close-up image of the target area with all objects is included in Fig. 6(a). The main radar parameters are listed in Table 1.



(a)



(b)

FIGURE 6. (a) Picture of the physical measurement scenario. (b) Schematic top-down view of the measurement scenario.

The positions of the repeater antennas as well as the ground truth position of all targets were measured using a total station. For the position of the radar antennas, information from a real-time kinematic global navigation satellite system (GNSS) was fused with data from an inertial measurement unit aboard the UAV [37].

A. SINGLE-TARGET EVALUATION

For the evaluation of the data, various measurement errors, inaccuracies and disturbances must be taken into account while performing data acquisition and evaluation. Avoiding or mitigating system-related disturbances to the received signal phase is a critical concern. Therefore, the scene is first populated only with the large cylinder [A].

1) STATIONARY RADAR MEASUREMENT

To visualize the effect of disturbances on the radar range evaluation, a stationary measurement was performed. During the measurement, the repeater was switched on and f_{mod} was

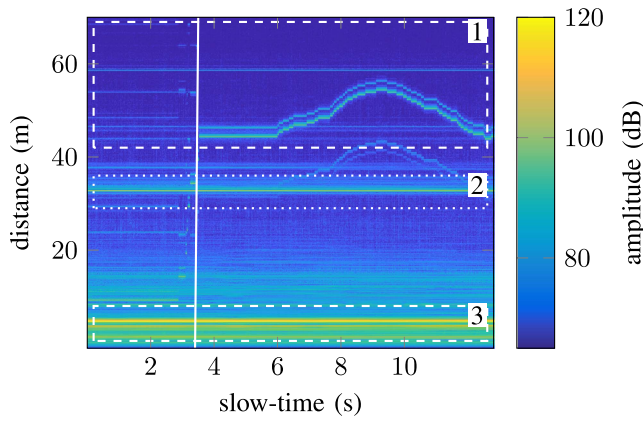


FIGURE 7. Plot of radar range over time. The radar range of target, repeater signal and of unwanted disturbances can be observed. Region 1: Bistatic, modulated signal; Region 2: Unwanted disturbances; Region 3: Monostatic signal.

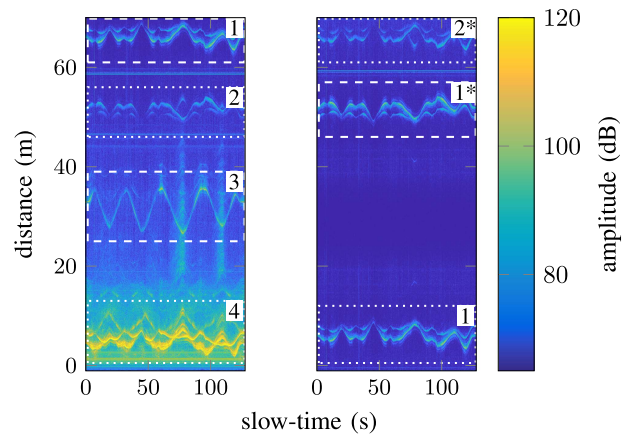


FIGURE 8. Measured range spectrum at UAV over slow-time t in case of a single target. Left: as received by the UAV. Right: after demodulation of the repeater signal.

varied, see Fig. 7. The modulation frequency of the repeater directly influences the virtual range of the bistatic targets. Although a single target was placed in the scene, two distinct closely spaced lines can be observed in region 1. This can be explained with the repeater as a target object in the scene. The modulated radar signal is not only transmitted to the target, but directly received by the radar. This line-of-sight component leads to an additional target, which is stronger than true bistatic targets observed via the repeater.

Beside the desired signal in region 1, region 2 shows a strong interfering signal, which could potentially mask the bistatic signal. Using a suitable f_{mod} , regions with strong interference signals can be avoided for the bistatic range evaluation. For the following measurements, the modulation frequency was set to $f_{\text{mod}} = 1.2$ MHz corresponding to a bistatic range shift of $R_{\text{shift}} = 60$ m, as described in (23).

Beyond 60 m no strong interferers were present during the measurements. The mixing process in the repeater results in the desired signals, but also includes other unwanted signal terms, such as the carrier signal, harmonics, and intermodulation products. The terms present after the mixing process are given by

$$f_{\text{out}} = \{n \cdot f_{\text{in}} \pm m \cdot f_{\text{mod}}\}, \quad n, m \in \mathbb{N}^0, \quad (28)$$

where f_{in} is the frequency of a signal received by the repeater and f_{out} is a set containing all theoretical frequency components resulting from f_{in} after the mixing process. In case of the used IQ-mixer, the undesired sideband ($f_{\text{in}} + f_{\text{mod}}$) is dampened, but still visible. Due to its shift in range, no disturbance of the bistatic signal is to be expected.

2) BISTATIC SAR

For this section, the UAV system is periodically moved back and forth on a linear trajectory, see Fig. 6. All occurring signal components are again visible in the range evaluation plot (left side of Fig. 8).

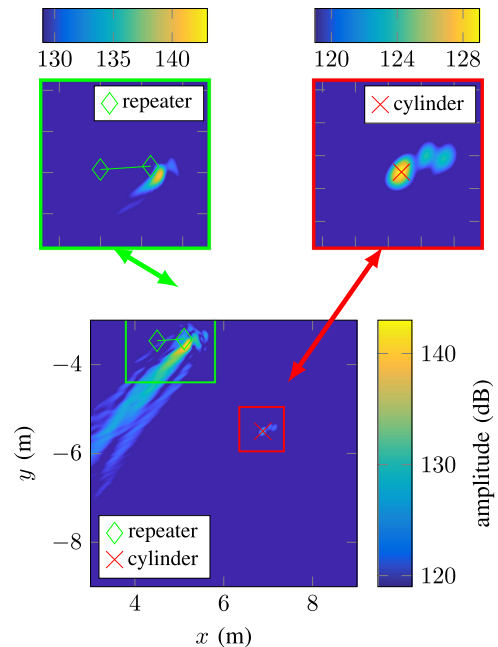


FIGURE 9. Bistatic SAR image of a scene with one cylinder target. A closer look on the areas where the target and repeater are located is given above the main image to show more details. The ground truth position of repeater antennas and target position is shown as green diamonds and red crosses respectively.

The varying distance of the UAV to the target is visible as a periodic shape in the radar range. The 60 m shift via the repeater leads to a bistatic received target range as observed in region 1. Region 2 contains the dampened sideband. The corresponding monostatic target range progression over time can be seen in region 4. The signal in region 3 is an artifact generated by the radar itself. Both regions 2 and 3 do not interfere with the measurements and can be disregarded, because there is no overlap with mono- or bistatic target responses for relevant radar ranges.

On the right side of Fig. 8 the range-compression after the demodulation is shown. Region 4 containing the monostatic

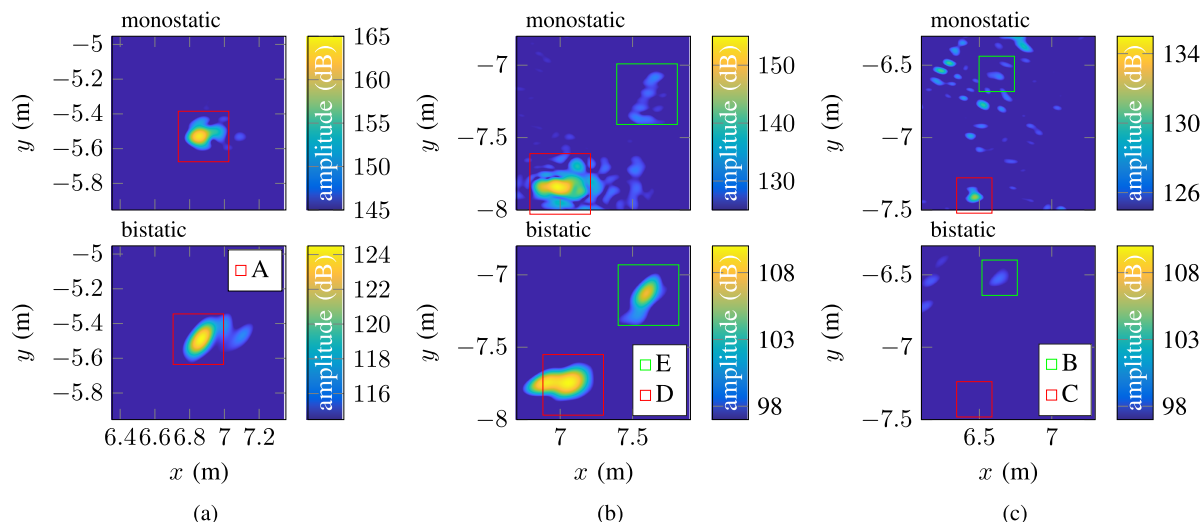


FIGURE 10. Comparison of the SAR images of the targets featured in Fig. 6. (a) Big cylinder [A]. (b) Small cylinder [E] and big sphere [D]. (c) Small aluminum ball [C] and corner reflector [B].

signal is no longer visible, because it is moved to negative frequencies. The signals in regions 1* and 2* are mirrored copies of 1 and 2, respectively and occur due to aliasing, see Fig. 2.

Using these demodulated range-compressed data and recorded localization information, the SAR image is processed and displayed in Fig. 9. The cylinder target [A] can be detected bistatically with high precision. Due to the implicit target generated by the repeater itself, a second peak is observed in the computed SAR image close to the location of the transmitting repeater antenna.

This result demonstrates the viability of repeater-based bistatic SAR processing. The benefit of the multiperspectivity on any given target via the repeater is further discussed in the next subsection.

B. MULTI-TARGET EVALUATION

Measurements are again performed monostatically and bistatically with additional metal objects [B-E] placed in the scene, as displayed in Fig. 6. An excerpt of the results of range-compression before and after demodulation is displayed in Fig. 11. Between mono- and bistatic measurements, there is a large difference in received power. In both cases, the varying range of multiple targets can be seen in the images.

The SAR evaluations of all target types is given in Fig. 10. To enable an accurate comparison between the monostatic and bistatic cases, the SAR images are further analyzed.

A statistical analysis of pixels in the target area is performed. Pixels containing higher power levels due to a target or because of imaging artifacts close to strong targets caused by the short linear aperture are excluded. For the remaining pixels, the amplitude in dB is extracted. From these amplitudes, a probability density estimate (PDE) is calculated using kernel density estimation.

This distribution is bell-shaped and its maximum value occurs at a certain amplitude value which will be referred to as the background level. Due to the difference in received

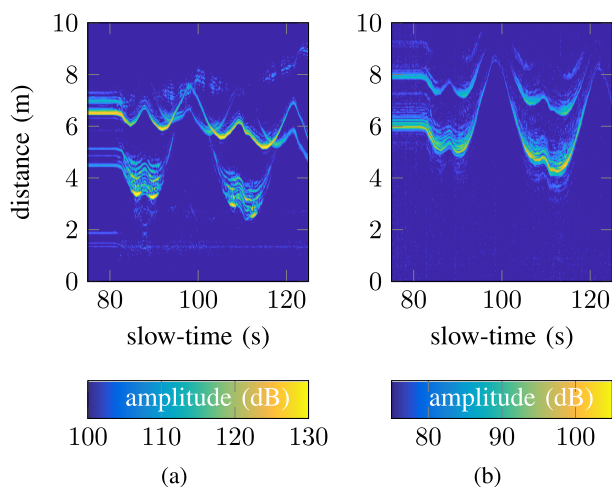


FIGURE 11. Range-compression for the multi-target case. (a) Monostatic signal, (b) Bistatic signal after demodulation.

power between mono- and bistatic images, the background level differs for the two cases. By normalizing the amplitude values to their respective background level, the distributions can be superimposed in a single plot (see Fig. 12).

Dividing the maximum amplitude of a target by the background level results in a signal-to-background ratio (SBR) for each target, which is additionally displayed in Fig. 12. Since the shape and width of the PDEs of the images is very similar, this measure enables a direct comparison between the monostatic and bistatic setup, regardless of the difference in overall received power.

In contrast, the SAR images allow for a comparison of the target within its surrounding area. Also, the shape of the target responses can be compared. Both representations have certain advantages. The following analysis therefore relies on both representations. A comparison of estimated target RCS

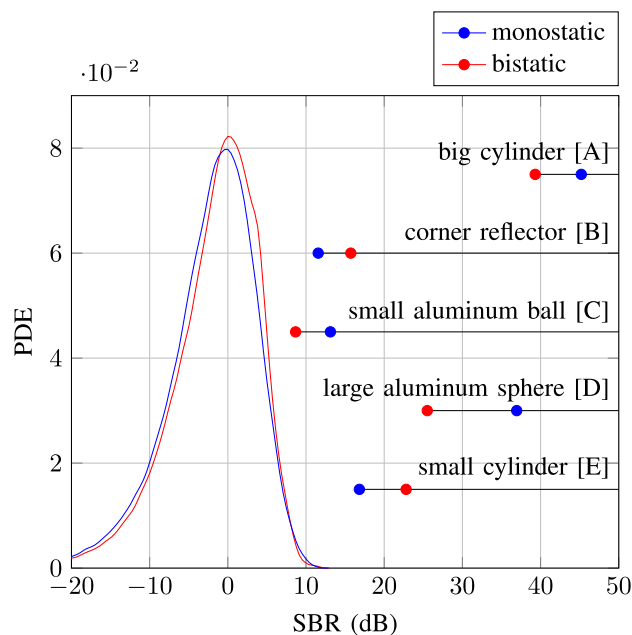


FIGURE 12. Probability density estimate of background distribution and target SBR for the monostatic and bistatic scenario and multiple targets.

is performed using the SBR, while heightened clutter level in an area is deduced directly from the SAR images.

Target A is again the large metal cylinder and serves as the reference target, since it yields the highest amplitude in mono- and bistatic evaluations. As expected, the cylinder has a large mono- and bistatic RCS. Target D is a large sphere covered in aluminum foil. This also results in a large mono- and bistatic RCS.

Target B is a small corner reflector. Its monostatic RCS is large in comparison to the bistatic one. Nevertheless, the reflector is not visible in the monostatic SAR image. This is mainly due to the measurement geometry, that resulted in target B overlapping target A at very similar ranges throughout the aperture. This leads to the same problem illustrated in Section III-A for repeaters without frequency modulation. Therefore the target is not visible, but a heightened clutter level is observed around the target location, which is again similar to the situation described above. In the bistatic case, the geometry is different and the overlap between targets A and B is reduced, resulting in a very weak target peak at the expected location, leading to an increased SBR.

Target C consists of a small ball of crumpled aluminum foil. Its monostatic RCS is small in comparison to the previous targets, but the target is still visible in the SAR image. In the bistatic image, this target cannot be detected, because the bistatic RCS is small due to strong scattering at the rough ball surface. This is confirmed by its low bistatic SBR.

Target E is a horizontally placed smaller metal cylinder. Due to its positioning, its RCS is larger in a bistatic scenario, which can be observed in the corresponding SAR images. In contrast to the previous targets, this leads to a bistatic SBR larger than the monostatic SBR.

V. CONCLUSION

This work demonstrates the BR-SAR concept using an active repeater element to enable simultaneous monostatic and bistatic SAR imaging with only a single radar sensor. The repeater receives the radar signal and modulates it using a mixer, which allows for a clean separation between monostatic and bistatic radar responses in signal processing.

Therefore, both mono- and bistatic SAR images can be generated from the same measurement data. The practical implementation of BR-SAR could be demonstrated in realistic measurements, leading to both monostatic and bistatic high-resolution SAR images. Additionally, it could be demonstrated that objects with larger bistatic RCS result in a higher amplitude in BR-SAR and are therefore easier to detect than using monostatic SAR. This improves detection performance and supplies additional target information.

REFERENCES

- [1] A. Moreira, P. Prats-Iraola, M. Younis, G. Krieger, I. Hajnsek, and K. P. Papathanassiou, "A tutorial on synthetic aperture radar," *IEEE Geosci. Remote Sens. Mag.*, vol. 1, no. 1, pp. 6–43, Mar. 2013.
- [2] S. Brusch, S. Lehner, T. Fritz, M. Soccorsi, A. Soloviev, and B. van Schie, "Ship surveillance with TerraSAR-X," *IEEE Trans. Geosci. Remote Sens.*, vol. 49, no. 3, pp. 1092–1103, Mar. 2011.
- [3] D. Brunner, G. Lemoine, and L. Bruzzone, "Earthquake damage assessment of buildings using VHR optical and SAR imagery," *IEEE Trans. Geosci. Remote Sens.*, vol. 48, no. 5, pp. 2403–2420, May 2010.
- [4] G. Fornaro, F. Lombardini, and F. Serafino, "Three-dimensional multipass SAR focusing: Experiments with long-term spaceborne data," *IEEE Trans. Geosci. Remote Sens.*, vol. 43, no. 4, pp. 702–714, Apr. 2005.
- [5] X. X. Zhu and R. Bamler, "Very high resolution spaceborne SAR tomography in urban environment," *IEEE Trans. Geosci. Remote Sens.*, vol. 48, no. 12, pp. 4296–4308, Dec. 2010.
- [6] G. Krieger et al., "TanDEM-X: A satellite formation for high-resolution SAR interferometry," *IEEE Trans. Geosci. Remote Sens.*, vol. 45, no. 11, pp. 3317–3341, Nov. 2007.
- [7] A. Moreira et al., "TanDEM-L: A highly innovative bistatic SAR mission for global observation of dynamic processes on the Earth's surface," *IEEE Geosci. Remote Sens. Mag.*, vol. 3, no. 2, pp. 8–23, Jun. 2015.
- [8] N. Pierdicca, L. Pulvirenti, F. Ticconi, and M. Brogioni, "Radar bistatic configurations for soil moisture retrieval: A simulation study," *IEEE Trans. Geosci. Remote Sens.*, vol. 46, no. 10, pp. 3252–3264, Oct. 2008.
- [9] V. Zavorotny et al., "Seasonal polarimetric measurements of soil moisture using tower-based GPS bistatic radar," in *Proc. IEEE Int. Geosci. Remote Sens. Symp.*, 2003, pp. 781–783.
- [10] J. L. Garrison, A. Komjathy, V. U. Zavorotny, and S. J. Katzberg, "Wind speed measurement using forward scattered GPS signals," *IEEE Trans. Geosci. Remote Sens.*, vol. 40, no. 1, pp. 50–65, Jan. 2002.
- [11] I. Walterscheid and A. R. Brenner, "Multistatic and multi-aspect SAR data acquisition to improve image interpretation," in *Proc. IEEE Int. Geosci. Remote Sens. Symp.*, 2013, pp. 4194–4197.
- [12] M. Stefko, O. Frey, C. Werner, and I. Hajnsek, "Calibration and operation of a bistatic real-aperture polarimetric-interferometric Ku-Band radar," *IEEE Trans. Geosci. Remote Sens.*, vol. 60, 2022, Art. no. 5106719.
- [13] M. Pieraccini, L. Miccinesi, and N. Rojhani, "A GBSAR operating in monostatic and bistatic modalities for retrieving the displacement vector," *IEEE Geosci. Remote Sens. Lett.*, vol. 14, no. 9, pp. 1494–1498, Sep. 2017.
- [14] M. Gottinger et al., "Coherent automotive radar networks: The next generation of radar-based imaging and mapping," *IEEE J. Microwaves*, vol. 1, no. 1, pp. 149–163, Jan. 2021.
- [15] M. García-Fernández, G. Álvarez-Narciandi, Y. Á. López, and F. L.-H. Andrés, "Analysis and validation of a hybrid forward-looking down-looking ground penetrating radar architecture," *Remote Sens.*, vol. 13, no. 6, Mar. 2021, Art. no. 1206.

- [16] A. Frischen, G. Hakobyan, and C. Waldschmidt, "Coherent measurements with MIMO radar networks of incoherent FMCW sensor nodes," *IEEE Microw. Wireless Compon. Lett.*, vol. 30, no. 7, pp. 721–724, Jul. 2020.
- [17] G. Krieger et al., "MirrorSAR: A fractionated space radar for bistatic, multistatic and high-resolution wide-swath SAR imaging," in *Proc. IEEE Int. Geosci. Remote Sens. Symp.*, 2017, pp. 149–152.
- [18] B. Meinecke, M. Steiner, J. Schlichenmaier, J. Hasch, and C. Waldschmidt, "Coherent multistatic MIMO radar networks based on repeater tags," *IEEE Trans. Microw. Theory Techn.*, vol. 67, no. 9, pp. 3908–3916, Sep. 2019.
- [19] D. Werbunat, B. Meinecke, B. Schweizer, J. Hasch, and C. Waldschmidt, "OFDM-Based radar network providing phase coherent DOA estimation," *IEEE Trans. Microw. Theory Techn.*, vol. 69, no. 1, pp. 325–336, Jan. 2021.
- [20] B. Meinecke, M. Steiner, J. Schlichenmaier, and C. Waldschmidt, "Instantaneous target velocity estimation using a network of a radar and repeater elements," in *Proc. IEEE 16th Eur. Radar Conf.*, 2019, pp. 241–244.
- [21] S. Appel, D. Berges, D. Mueller, A. Ziroff, and M. Vossiek, "MIMO FMCW reader concept for locating backscatter transponders," *IEEE Trans. Microw. Theory Techn.*, vol. 64, no. 9, pp. 2955–2967, Sep. 2016.
- [22] M. Pieraccini and L. Miccinesi, "Bistatic ArcSAR," in *Proc. IEEE 2nd URSI Atlantic Radio Sci. Meeting*, 2018, pp. 1–4.
- [23] L. Miccinesi, L. Bigazzi, M. Pieraccini, and M. Basso, "Bistatic GB-SAR with moving transponder," in *Proc. IEEE 18th Eur. Radar Conf.*, 2022, pp. 353–356.
- [24] P. Hügler, F. Roos, M. Schartel, M. Geiger, and C. Waldschmidt, "Radar taking off: New capabilities for UAVs," *IEEE Microw. Mag.*, vol. 19, no. 7, pp. 43–53, Nov./Dec. 2018.
- [25] A. Grathwohl et al., "Taking a look beneath the surface: Multicopter UAV-based ground-penetrating imaging radars," *IEEE Microw. Mag.*, vol. 23, no. 10, pp. 32–46, Oct. 2022.
- [26] I. Catapano, G. Gennarelli, G. Ludeno, C. Noviello, G. Esposito, and F. Soldovieri, "Contactless ground penetrating radar imaging: State of the art, challenges, and microwave tomography-based data processing," *IEEE Geosci. Remote Sens. Mag.*, vol. 10, no. 1, pp. 251–273, Mar. 2022.
- [27] Y. A. Lopez, M. Garcia-Fernandez, G. Alvarez-Narciandi, and F. L.-H. Andres, "Unmanned aerial vehicle-based ground-penetrating radar systems: A review," *IEEE Geosci. Remote Sens. Mag.*, vol. 10, no. 2, pp. 66–86, Jun. 2022.
- [28] M. Schartel, R. Burr, W. Mayer, N. Docci, and C. Waldschmidt, "UAV-based ground penetrating synthetic aperture radar," in *Proc. IEEE MTT-S Int. Conf. Microw. Intell. Mobility*, 2018, pp. 1–4.
- [29] M. Schartel, K. Prakasan, P. Hugler, R. Burr, W. Mayer, and C. Waldschmidt, "A multicopter-based focusing method for ground penetrating synthetic aperture radars," in *Proc. IEEE Int. Geosci. Remote Sens. Symp.*, 2018, pp. 5420–5423.
- [30] S. Prager, G. Sexstone, D. McGrath, J. Fulton, and M. Moghaddam, "Snow depth retrieval with an autonomous UAV-mounted software-defined radar," *IEEE Trans. Geosci. Remote Sens.*, vol. 60, 2022, Art. no. 5104816.
- [31] C. Noviello, G. Esposito, I. Catapano, and F. Soldovieri, "Multilines imaging approach for mini-UAV radar imaging system," *IEEE Geosci. Remote Sens. Lett.*, vol. 19, 2022, Art. no. 3507105.
- [32] E. C. Zaugg and D. G. Long, "Generalized frequency scaling and back-projection for LFM-CW SAR processing," *IEEE Trans. Geosci. Remote Sens.*, vol. 53, no. 7, pp. 3600–3614, Jul. 2015.
- [33] M. Schartel, R. Burr, R. Bähnemann, W. Mayer, and C. Waldschmidt, "An experimental study on airborne landmine detection using a circular synthetic aperture radar," 2020. [Online]. Available: <https://arxiv.org/abs/2005.02600>
- [34] V. Winkler, "Range doppler detection for automotive FMCW radars," in *Proc. IEEE Eur. Microw. Conf.*, 2007, pp. 1445–1448.
- [35] F. Yaman, C. Özdemir, Ş. Demirci, E. Yiğit, and B. Yilmaz, "A review on migration methods in B-scan ground penetrating radar imaging," *Math. Problems Eng.*, vol. 2014, 2014, Art. no. 280738.
- [36] D. J. Daniels, Ed., *Ground Penetrating Radar*, 2nd ed. Stevenage, U.K.: IET, 2007.
- [37] R. Bähnemann et al., "Under the sand: Navigation and localization of a micro aerial vehicle for landmine detection with ground penetrating synthetic aperture radar," 2021. [Online]. Available: <https://arxiv.org/abs/2106.10108>



ALEXANDER GRATHWOHL (Graduate Student Member, IEEE) received the master's degree in electrical engineering in 2019 from Ulm University, Ulm, Germany, where he is currently working toward the Ph.D. degree in electrical engineering with the Institute of Microwave Engineering with a focus on airborne GPSAR systems and their application for humanitarian demining. From 2017 to 2018, he was an intern with EAA, Bosch Sensortec, Sunnyvale, CA, USA.



BENEDIKT MEINECKE (Graduate Student Member, IEEE) received the M.Sc. degree in electrical engineering in 2017 with a focus on communication technology from Ulm University, Ulm, Germany, where he is currently working toward the Ph.D. degree in electrical engineering with the Institute of Microwave Engineering. His research interests include system concepts for multistatic coherent radar networks and the accompanying signal processing.



MARIUS WIDMANN is currently working toward the master's degree in electrical engineering with Ulm University, Ulm, Germany. Since 2021, he has been a student worker with the Institute of Microwave Engineering.



JULIAN KANZ (Graduate Student Member, IEEE) received the B.Sc. and M.Sc. degrees in electrical engineering in 2019 and 2022, respectively, from Ulm University, Ulm, Germany, where he is currently working toward the Ph.D. degree with the Institute of Microwave Engineering. His research interests include system concepts for multistatic radar networks on UAVs and high-resolution synthetic aperture radar processing.



CHRISTIAN WALDSCHMIDT (Fellow, IEEE) received the Dipl.-Ing. (M.S.E.E.) and Dr.-Ing. (Ph.D.E.E.) degrees from University Karlsruhe, Karlsruhe, Germany, in 2001 and 2004, respectively. From 2001 to 2004, he was a Research Assistant with the Institut für Höchstfrequenztechnik und Elektronik, Universität Karlsruhe. Since 2004, he has been with Robert Bosch GmbH, in the business units Corporate Research and Chassis Systems. He was heading different research and development teams in microwave engineering, RF-sensing, and automotive radar. In 2013, he returned to academia. He was appointed as the Director of the Institute of Microwave Engineering, University Ulm, Ulm, Germany, as a Full Professor. He has authored or coauthored more than 200 scientific publications and more than 20 patents. His research interests include radar and RF-sensing, mm-wave and submillimeter-wave engineering, antennas and antenna arrays, and RF and array signal processing. He is a member of the Executive Committee Board of the German MTT/AP joint chapter, and a member of the German Information Technology Society. He is Chair of the IEEE MTT-29 Technical Committee on Microwave Aerospace Systems and was Chair of the MTT-27 Technical Committee on Wireless Enabled Automotive and Vehicular Applications. He was a two-time TPC Chair and General Chair of the IEEE MTT International Conference on Microwaves for Intelligent Mobility. Since 2018, he has been an Associate Editor for IEEE MTT MICROWAVE WIRELESS COMPONENTS LETTERS. He is a reviewer of multiple IEEE transactions and many IEEE conferences in the field of microwaves. He was co-recipient of 11 best paper awards in 2014.